Carrier-phonon interaction in small cross-sectional silicon nanowires

A. K. Buin,[1] A. Verma,[2] and M. P. Anantram[1]
[1]*Department of Electrical and Computer Engineering, University of Waterloo, Waterloo, Ontario N2L 3G1, Canada*
[2]*Department of Electrical Engineering and Computer Science, Texas A&M University-Kingsville, Kingsville, Texas 78363, USA*

(Received 18 June 2008; accepted 24 June 2008; published online 10 September 2008)

Using first-order perturbation theory and deformation potential approximation, the interaction of electrons and holes with acoustic and optical phonons is investigated in silicon nanowires (SiNWs) with different diameters and crystallographic axis orientations. The electronic band structures for [110] and [100] SiNWs are obtained from a $sp^3d^5s^*$ tight-binding scheme, while a continuum model is assumed for phonon dispersion. The influence of confined and bulk phonons on carrier transport is investigated. © *2008 American Institute of Physics*. [DOI: 10.1063/1.2974088]

I. INTRODUCTION

Silicon nanowires (SiNWs) hold a significant potential for the continued successful scaling of semiconductor devices, and could play a critical role in future electronic and sensor applications. The band structure, and therefore the electronic properties, of SiNWs vary vastly with their physical structures,[1–3] which in turn requires a detailed characterization of all of them. Recent experimental work[4] suggests that the growth of freestanding small diameter [110] SiNWs (<10 nm) is thermodynamically favorable. Our recent work[5] suggests that acoustic phonon limited hole mobility in these dimensionally reduced structures significantly exceeds that of electrons, as well as acoustic phonon limited hole mobility in bulk silicon. At room temperature, hole carrier mobility in bulk silicon is however also influenced by optical phonons.[6,7] Therefore there is a need to explore the effect of optical phonon scattering on hole transport in small diameter SiNWs. Concomitantly, it is also important to undertake a comparison of low-field mobility calculations among SiNWs of similar diameters, but with different crystalline orientations and surface boundary conditions. This is because while many researchers have computed the low-field mobility of different SiNWs,[8–14] a comparison becomes difficult because of different models utilized. A significant majority of calculations have been undertaken for electron transport in nanowires[12–19] with emphasis on acoustical and polar-optical phonon scattering by ignoring real band structure effects. Simultaneously, to date there are limited data available for hole transport in small diameter SiNWs.[5,20,21] Investigation of hole transport in these structures in itself requires further detailed investigation because of recent experimental results that show an enhancement of hole mobility.[22] In particular, calculations should include detailed band structure and intersubband coupling between the relatively closely spaced valence subbands, as well as confined and bulk phonons. Confined phonons correspond to phonon modes in a wire of diameter equal to the diameter of the SiNW. Bulk phonons correspond to phonon modes in bulk silicon. This is further illustrated in Fig. 1

In this paper we present results on charge-phonon (acoustic and optical) interaction for SiNWs with different diameters, axis orientations, and boundary conditions. In particular, [110] and [100] axially aligned SiNWs are discussed and their phonon limited charge low-field mobility evaluated utilizing confined acoustic phonons under freestanding and clamped surface boundary conditions (FSBC and CSBC, respectively), as well as bulk acoustic and optical phonons. The band structure for the SiNWs is computed using a $sp^3d^5s^*$ tight-binding (TB) scheme. Carrier-phonon momentum relaxation rates are computed using first-order perturbation theory and deformation potential approximation. In computing all relaxation rates, electron and hole TB wave functions are employed.

This paper is divided into various sections. Section II A describes the method used to obtain the band structure, and the electron and hole wave functions. Section II B describes the method used to compute confined acoustic phonon dispersion. Section II C describes the evaluation of the momentum relaxation rates through bulk and confined phonons. Section III presents results on electron and hole low-field mobility values. Finally Sec. IV draws conclusions from the work and results mentioned.

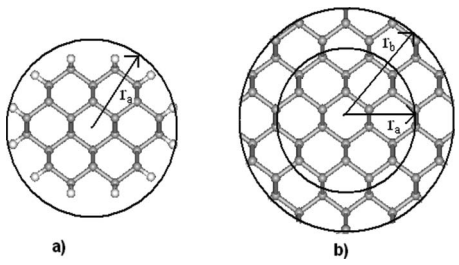


FIG. 1. Physical picture of (a) confined phonon box and (b) bulk phonons limit. r_a is the radius of the corresponding equivalent cylindrical box for confined phonons and electrons for (a), in case of (b) r_a is the electron confinement box, r_b is the radius of surrounding phonon box (in our case it is 32 nm). Note as $r_b \to \infty$, we reach bulk limit.

 © 2008 American Institute of Physics

Downloaded 16 Sep 2008 to 129.97.106.193. Redistribution subject to AIP license or copyright; see http://jap.aip.org/jap/copyright.jsp

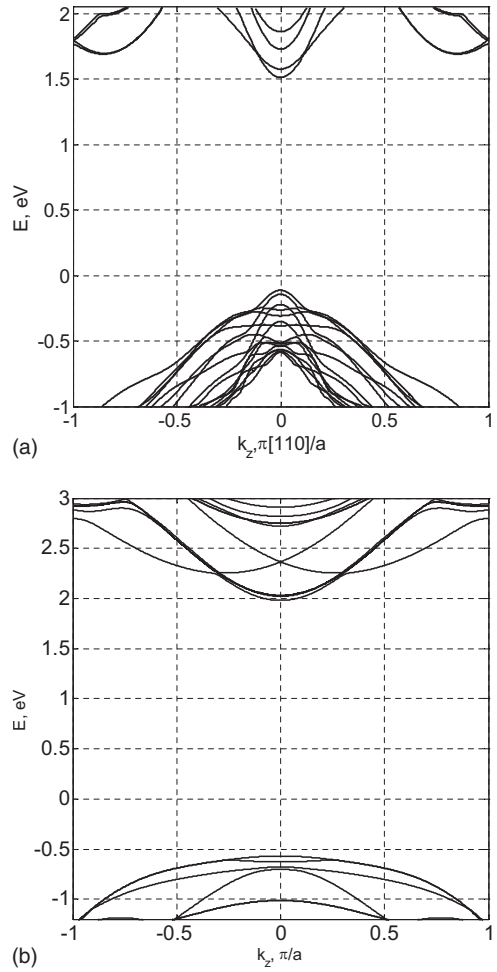


FIG. 2. (a) Band structure of a 2.47 nm diameter [110] SiNW. This figure is taken from Ref. 5. (b) Band structure of a 1.5 nm diameter [100] SiNW.

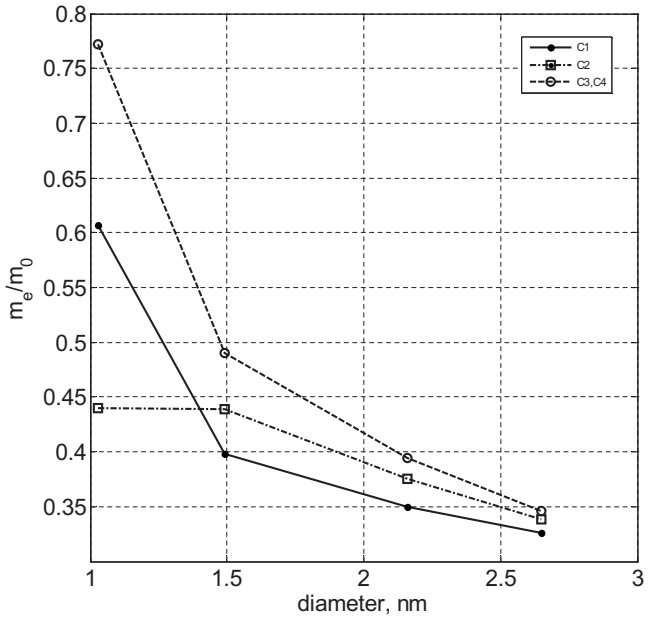


FIG. 3. Electron effective masses for [100] wires. C1–C4 are the four lowest conduction subbands.

II. METHODS AND THEORY

A. Band structure

The band structures for the hexagonal cross-sectional [110] and [100] SiNWs are obtained by utilizing the semiempirical $sp^3d^5s^*$ TB scheme,[23] where interaction with first nearest neighbors is considered. Within the TB scheme, all Si dangling bonds at the edges are passivated with hydrogen atoms in order to eliminate unphysical surface states. The TB parameters for the Si–Si bonds and for the Si–H bonds are obtained from Refs 23 and 24, respectively. Figure 2(a) shows the first few conduction and valence subbands for a 2.47 nm diameter [110] SiNW, while Fig. 2(b) shows the conduction and valence subbands for a 1.5 nm diameter [100] SiNW. The band structures thus obtained[5] are in agreement with Ref. 3. For the [110] SiNWs under consideration, the electron effective mass at the bottom of the first conduction subband is seen to increase with diameter from a low value of $0.167m_0$ to $0.185m_0$, where m_0 is the electron rest mass. The electron effective mass for the lowest conduction subband in [100] SiNWs decreases from $0.6m_0$ for a 1.0 nm diameter SiNW to $0.326m_0$ for a 2.65 nm diameter SiNW. A comparison in electron effective mass between [100] and [110] SiNWs for the lowest few conduction subbands can be made from Fig. 3 and Ref. 5. As the diameter of the SiNWs is increased further, the electron effective mass is expected to reach a value of silicon bulk transverse effective mass for both classes of SiNWs. Moreover, from the band structure calculations, [100] SiNW hole effective masses for the top valence subbands are also seen to be greater than the [110] SiNWs of similar diameters.

As also seen in Fig. 2(a), in addition to the conduction band minima at $k_z=0$ point, there are four additional satellite minima at $k_z \approx \pm 1.22\pi/a$, where a is the lattice constant for bulk silicon. The presence of these minima can be qualitatively understood in terms of mapping four equivalent minima in bulk silicon in [100] and [010] directions on the [110] direction. Within the bulk Si first Brillouin zone (BZ), there are six equivalent conduction valleys in the ⟨100⟩ directions. In confining bulk Si to a SiNW, two of those valleys lying on the axis normal to that of the SiNW give rise to the central minima, while the remaining four give rise to the satellite valleys observed in Fig. 2(a).

The electron and hole wave functions within the TB scheme for the SiNWs are given by

$$\psi_\nu(k_z,\mathbf{r}) = \frac{1}{\sqrt{N}}\sum_{n,m} c_\nu(k_z)e^{ik_z na_l}\varphi_m[\mathbf{r}-(\boldsymbol{\tau}_m \pm \mathbf{e_z}na_l)], \qquad (1)$$

where summation over n means summation over all unit cells, a_l is the SiNW lattice constant ($a_l=a$ for [100] SiNW and $a/\sqrt{2}$ for [110] SiNWs, where a is the lattice constant for bulk Si), ν is the subband index, k_z is the electron wave vector along the SiNW axis z, $\mathbf{r}$ is the radius vector, N is the number of unit cells, m represents orbital and location, $\boldsymbol{\tau}_m$ is the location of atom within the unit cell, φ_m are orthonormal atomic orbitals, c_ν are expansion coefficients whose values are obtained within the TB scheme,[25] and $\mathbf{e_z}$ is the unit vector along the SiNW axis.

Downloaded 16 Sep 2008 to 129.97.106.193. Redistribution subject to AIP license or copyright; see http://jap.aip.org/jap/copyright.jsp

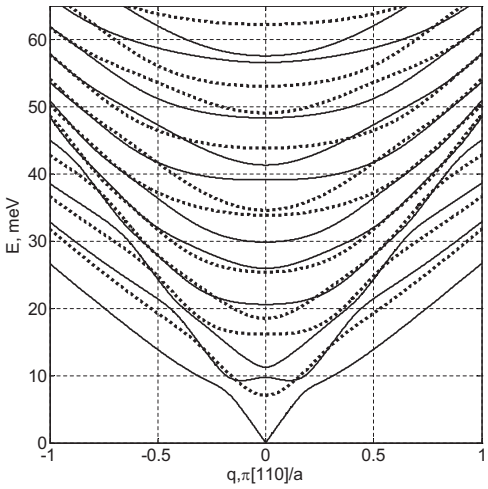


FIG. 4. Confined dilatational modes for 2.47 nm diameter [110] SiNW, in case of freestanding wire and clamped wire (solid lines are for freestanding wire, dashed lines are for clamped wire). Note that a linear phonon mode does not exist for the clamped wire.

B. Confined phonon dispersion

As described in our previous work,[5] in order to obtain confined acoustic phonon dispersion, we consider SiNWs embedded within a circular phonon box of radius r. Dispersion relationship for a coupled axial-radial dilatational mode for a FSBC is obtained from the elastic wave equation and given by the Pochhammer–Chree equation[26]

$$\frac{2k_l}{r}(q^2+k_t^2)J_1(k_l r)J_1(k_t r)-(k_t^2-q^2)^2J_0(k_l r)J_1(k_t r) - 4q^2k_lk_tJ_1(k_l r)J_0(k_t r)=0, \tag{2}$$

where r is the radius of the phonon box, q is the phonon wave vector along axis of the SiNW, and J_0 and J_1 are Bessel functions of the first kind. For a given axial wave vector q we find the lowest 15 modes for energy $\omega_n(q)$. The values of k_l and k_t that correspond to $\omega_n(q)$ are represented by $k_{l,n}$ and $k_{t,n}$. $\omega_n(q)$, $k_{l,n}$, and $k_{t,n}$ are related by $k_{l,n}^2=\omega_n^2/\upsilon_l^2-q^2$ and $k_{t,n}^2=\omega_n^2/\upsilon_t^2-q^2$. υ represents the acoustic velocity with subscripts t and l standing for transverse and longitudinal, respectively. We take $\upsilon_t=5.5\times10^5$cm/s and $\upsilon_l=9.01\times10^5$cm/s. In the limit of a large radius r, we approach bulk acoustic phonon dispersion. For the case of a CSBC, the confined acoustic phonon dispersion becomes

$$k_lk_tJ_1(k_l r)J_0(k_t r)+q^2J_1(k_t r)J_0(k_l r)=0. \tag{3}$$

The relationship between $\omega_n(q)$, $k_{l,n}$, and $k_{t,n}$ are the same as discussed above. The above equations can be solved numerically to obtain $\omega_n(q)$. Figure 4 shows the dilatational phonon dispersion for the 2.47 nm diameter [110] SiNW using the FSBC and CSBC equations. As can be seen from the figure, clamping the boundary results in the disappearance of the nearly linear phonon mode. This in turn results in an increase in carrier mobility as has been reported in Ref. 27.

The atomic displacements due to the above acoustic phonons are given by[26]

$$u_{r,n}=[iqC_nJ_1(k_{t,n}\rho)-k_lA_nJ_1(k_{l,n}\rho)]e^{i(qz-\omega_n t)},$$
$$u_{z,n}=[iqA_nJ_0(k_{l,n}\rho)-k_tC_nJ_0(k_{t,n}\rho)]e^{i(qz-\omega_n t)}, \tag{4}$$

where $A_n=r/2\sqrt{[\hbar/\rho V\omega_n(q)\gamma_n]}$, and

$$\gamma_n=\frac{q^2r^2}{2}[J_1(k_{l,n}r)^2+J_0(k_{l,n}r)^2]+\frac{\beta^2k_{t,n}^2r^2}{2}[J_1(k_{t,n}r)^2 + J_0(k_{t.n}r)^2]+\frac{k_{l,n}^2r^2}{2}[J_1(k_{l,n}r)^2-J_0(k_{l,n}r)J_2(k_{l,n}r)] + \frac{\beta_n^2q^2r^2}{2}[J_1(k_{t,n}r)^2-J_0(k_{t,n}r)J_2(k_{t,n}r)] + \frac{2\beta_nqk_{l,n}r}{(k_{l,n}^2-k_{t,n}^2)}[k_{l,n}J_0(k_{l,n}r)J_1(k_{t,n}r) - k_{t,n}J_0(k_{t,n}r)J_1(k_{l,n}r)] - \frac{2\beta_nqk_{t,n}r}{(k_{l,n}^2-k_{t,n}^2)}[k_{t,n}J_0(k_{l,n}r)J_1(k_{t,n}r) - k_{l,n}J_0(k_{t,n}r)J_1(k_{l,n}r)]. \tag{5}$$

The ratio β_n is given as

$$\beta_n=C_n/A_n=-\frac{2qk_{l,n}}{(k_{t,n}^2-q^2)}\frac{J_1(k_{l,n}r)}{J_1(k_{t,n}r)}, \quad \text{for FSBC,} \quad \text{and}$$

$$\beta_n=C_n/A_n=\frac{k_{l,n}}{q}\frac{J_1(k_{l,n}r)}{J_1(k_{t,n}r)}, \quad \text{for CSBC,} \tag{6}$$

and the constant A_n is obtained through normalization of the phonon modes[28] as

$$\frac{1}{\pi r^2}\int_0^r\int_0^{2\pi}\mathbf{u}_m^*(\rho,z)\mathbf{u}_n(\rho,z)\rho d\rho d\varphi = \begin{cases}\hbar/2M\omega_n(q), & m=n\\ 0, & m\neq n\end{cases}. \tag{7}$$

C. Momentum relaxation rates

The charge scattering rates due to phonons are calculated from Fermi's golden rule and deformation potential approximation[29] as

$$W_{\mu,\nu}(k_z,k_z',\tilde{\mathbf{q}}) = \frac{2\pi}{\hbar}\left|\left\langle\psi_\nu(k_z'),N_{|\tilde{\mathbf{q}}|}+\frac{1}{2}\pm\frac{1}{2}\middle|H_{\tilde{\mathbf{q}},e-ph}\middle|\psi_\mu(k_z),N_{|\tilde{\mathbf{q}}|}\right\rangle\right|^2 \times\delta[E_\nu(k_z')-E_\mu(k_z)\pm\hbar\omega(|\tilde{\mathbf{q}}|)], \tag{8}$$

where k_z and k_z' are the initial and final crystal momenta, respectively, $N_{|\tilde{\mathbf{q}}|}$ is the phonon equilibrium Bose–Einstein occupation number, μ and ν are initial and final subbands, respectively, δ is the Dirac delta function, and $\tilde{\mathbf{q}}$ is the phonon wave vector. $\tilde{\mathbf{q}}=(q_t,q)$, where q is the axial phonon wave vector and q_t is the projection of $\tilde{\mathbf{q}}$ onto the confine-

Downloaded 16 Sep 2008 to 129.97.106.193. Redistribution subject to AIP license or copyright; see http://jap.aip.org/jap/copyright.jsp

ment plane, and −/+ corresponds to phonon absorption/emission.

The charge-phonon interaction Hamiltonian in case of bulk phonons in second quantized form is given by

$$H_{\tilde{\mathbf{q}},e-ph} = iE_a \sum_{\tilde{\mathbf{q}}} |\tilde{\mathbf{q}}| \sqrt{\frac{\hbar}{2\rho V \omega(|\tilde{\mathbf{q}}|)}} (a_{\tilde{\mathbf{q}}} + a^{\dagger}_{-\tilde{\mathbf{q}}}) e^{i\tilde{\mathbf{q}}\mathbf{r}} \tag{9}$$

where $a_{\tilde{\mathbf{q}}}$ and $a^{\dagger}_{-\tilde{\mathbf{q}}}$ are phonon annihilation and creation operators, respectively, E_a is the deformation potential, ρ is the SiNW mass density, V is the volume of the SiNW, $\omega(|\tilde{\mathbf{q}}|)$ is the phonon frequency, and $|\tilde{\mathbf{q}}| = \sqrt{q^2 + q_t^2}$. Utilizing the electron wave functions within the TB scheme given by Eq. (1), the matrix element in Eq. (8) becomes

$$\begin{aligned} &\left| \left\langle \psi_\nu(k_z'), N_{|\tilde{\mathbf{q}}|} + \frac{1}{2} \pm \frac{1}{2} | H_{\tilde{\mathbf{q}},e-ph} | \psi_\mu(k_z), N_{|\tilde{\mathbf{q}}|} \right\rangle \right| \\ &= \delta_{k_z', k_z \pm q} |\tilde{\mathbf{q}}| E_a \left[\frac{\hbar}{2\rho V \omega(|\tilde{\mathbf{q}}|)} \right]^{1/2} \\ &\times \left(N_{|\tilde{\mathbf{q}}|} + \frac{1}{2} \pm \frac{1}{2} \right)^{1/2} \sum_{m,m'} c_{\mu,m}(k_z) c^*_{\nu,m'}(k_z') \\ &\times [G_{m,m'}(0,0) + e^{\pm i a_l z} G_{m,m'}(0, \pm 1)], \end{aligned} \tag{10}$$

where δ is the Kronecker delta function and

$$\begin{aligned} G_{m,m'}(0,0) &= \int \varphi^*_{m'}(\mathbf{r} - \boldsymbol{\tau}_{m'}) e^{i\mathbf{q}\mathbf{r}} \varphi_m(\mathbf{r} - \boldsymbol{\tau}_m) d^3 r, \\ G_{m,m'}(0, \pm 1) &= \int \varphi^*_{m'}[\mathbf{r} - (\boldsymbol{\tau}_{m'} \pm \mathbf{e}_z a_l)] e^{i\mathbf{q}\mathbf{r}} \varphi_m(\mathbf{r} - \boldsymbol{\tau}_m) d^3 r. \end{aligned} \tag{11}$$

In deriving Eq. (10) it is assumed that the coupling between non-neighboring unit cells is insignificant compared to neighboring unit cells. Also, $\sum_{n=1}^{N} e^{-i(k_z' - k_z \pm q) n a_l} = N \delta_{k_z', k_z \pm q}$. We take integrals between orbitals: (i) of different type on the same atom and (ii) on different atoms to be zero. In addition, terms of the form $\int \varphi^*_m(\mathbf{r} - \boldsymbol{\tau}_{m'}) e^{i\mathbf{q}(\mathbf{r} - \boldsymbol{\tau}_m)} \varphi_m(\mathbf{r} - \boldsymbol{\tau}_m) d^3 r$ are taken to be unity. This is a reasonable approximation when $2\pi/q$ is much larger than the span of orbital m. As a result, Eq. (10) reduces to

$$\begin{aligned} &\left| \left\langle \psi_\nu(k_z'), N_{|\tilde{\mathbf{q}}|} + \frac{1}{2} \pm \frac{1}{2} | H_{\tilde{\mathbf{q}},e-ph} | \psi_\mu(k_z), N_{|\tilde{\mathbf{q}}|} \right\rangle \right| \\ &= \delta_{k_z', k_z \pm q} |\tilde{\mathbf{q}}| E_a \left[\frac{\hbar}{2\rho V \omega(|\tilde{\mathbf{q}}|)} \right]^{1/2} \left(N_{|\tilde{\mathbf{q}}|} + \frac{1}{2} \pm \frac{1}{2} \right)^{1/2} S(\tilde{\mathbf{q}}), \end{aligned} \tag{12}$$

where S is the overlap factor that indicates momentum conservation in the confined direction and is given by

$$S_{\mu,\nu}(\tilde{\mathbf{q}}) = \sum_m c_{\mu,m}(k_z) c^*_{\nu,m}(k_z') e^{i\tilde{\mathbf{q}}\boldsymbol{\tau}_m}. \tag{13}$$

Once the matrix elements are computed one can compute the momentum relaxation rates. In the case of bulk acoustic phonons, as the length of the SiNW increases, the number of phonon modes approaches infinity. In this case sum over phonon modes becomes an integration,

$$\sum_{\tilde{\mathbf{q}}} \sum_{k_z'} \rightarrow \frac{V}{(2\pi)^3} \int \int \int q_t dq_t d\varphi dq.$$

Bulk acoustic phonon dispersion is taken to be linear within the Debye approximation, with a dispersion $\omega(|\tilde{\mathbf{q}}|) = \upsilon_l |\tilde{\mathbf{q}}|$, where longitudinal sound velocity is given above. With the aid of Dirac delta function and the discrete momentum conserving delta function along the SiNW axis one obtains the carrier momentum relaxation rates from initial subband μ to final subband ν as[5]

$$\begin{aligned} W_{\mu,\nu}(k_z) &= \sum_{k_z', \tilde{\mathbf{q}}} W_{\mu,\nu}(k_z', k_z, \tilde{\mathbf{q}}) \left(1 - \frac{k_z'}{k_z} \right) \\ &= -\frac{E_a^2}{4\pi\hbar^3 \rho \upsilon_s^4} \int_\Omega \Delta E_{\mu,\nu}(k_z \pm q)^2 S_{1,\mu,\nu}(q_n, k_z \pm q) \\ &\times \left(N_{|\tilde{\mathbf{q}}|} + \frac{1}{2} \pm \frac{1}{2} \right) \frac{q}{k_z} dq, \end{aligned} \tag{14}$$

where $\Delta E_{\mu,\nu} = E_\nu(k_z') - E_\mu(k_z)$ is the energy difference between initial and final subbands, μ and ν, respectively. Also, $q_n = \sqrt{(\Delta E_{\mu,\nu}(k_z \pm q)/\hbar\upsilon_l)^2 - q^2}$ and $S_{1,\mu,\nu} = 1/2\pi \times \int_0^{2\pi} |S_{\mu,\nu}(\tilde{\mathbf{q}})|^2 d\varphi$. The bulk Debye energy $E_D = 55$ meV (Ref. 30) is utilized to define the domain of integration Ω. In obtaining the above momentum relaxation rates prescription we have neglected Umklapp processes. The overlap factor is given by

$$\begin{aligned} S_{1,\mu,\nu}(q_t, k_z) &= \sum_m |c_{\mu,m}(k_z)|^2 |c_{\nu,m}(k_z')|^2 + \sum_{m,m',m \neq m'} A_{m,m'} J_0 \\ &\times (q_t \sqrt{\Delta x_{m,m'}^2 + \Delta y_{m,m'}^2}) e^{-iq\Delta z_{m,m'}}, \end{aligned} \tag{15}$$

where $A_{m,m'} = c_{\mu,m}(k_z) c^*_{\nu,m}(k_z') c^*_{\mu,m'}(k_z) c_{\nu,m'}(k_z')$, and $\Delta j_{m,m'} = (j_m - j_{m'})$, where j is x, y, or z.

While the overlap factor prescription (15) holds in general for any number of subbands, it can be further simplified for intrasubband electron scattering for the first conduction subband

$$S_{\mu,\nu}(q_t, k_z) = \sum_m c_{\mu,m}(k_z) c^*_{\nu,m}(k_z') J_0(q_t \rho_m) e^{iqz_m}, \tag{16}$$

where we have used

$$e^{i\tilde{\mathbf{q}}\boldsymbol{\tau}_m} = e^{iqz_m} [J_0(q_t\rho_m) + 2\sum_{n=1}^{\infty} i^n J_n(q_t\rho_m) \cos(n\varphi_m)], \tag{17}$$

where ρ_m and z_m are the radial and axial locations of the atom m in cylindrical coordinates. Note that the second term of the right hand side of Eq. (17) does not contribute to Eq. (16) because the first conduction subband state is symmetric with respect to φ_m. As the $\cos(n\varphi_m)$ terms contribute to higher order modes, one should use Eq. (15) instead of Eq. (16) when occupancy in subbands two and higher becomes substantial.

For confined acoustic phonons, the charge-phonon interaction Hamiltonian is given as[31]

Downloaded 16 Sep 2008 to 129.97.106.193. Redistribution subject to AIP license or copyright; see http://jap.aip.org/jap/copyright.jsp

$$H_{e\text{-ph}} = E_a \nabla \cdot \mathbf{u} = E_a \sum_n \sum_q A_n (q^2 + k_{l,n}^2) J_0(k_{l,n} r)(a_q + a_{-q}^+) e^{iqz}. \quad (18)$$

The matrix element can be obtained by using a similar procedure followed for the bulk scattering case discussed above where $S_{\mu,\nu}(q)$ is given by Eq. (16), but with q_t replaced by $k_{l,n}$. Using this and utilizing the transformation $\sum_{k_z'} \rightarrow L/2\pi \int dq$, one can then obtain the carrier momentum relaxation rates from confined acoustic phonons as

$$W_{\mu,\nu}(k_z) = \sum_{k_z',q,n} W_{\mu,\nu}(k_z', k_z, q, n)\left(1 - \frac{k_z'}{k_z}\right) = -\frac{E_a^2}{4\pi\hbar^3 \rho v_s^4} \sum_n \sum_p \frac{q_p}{k_z} \gamma^{-1} \left(N_q + \frac{1}{2} \pm \frac{1}{2}\right) \times |S_{\mu,\nu}(k_{l,n}, q_p)|^2 E_{\text{ph}}^3(q_p) \text{JDOS}_\nu(k_z, q_p), \quad (19)$$

with

$$W_{\mu,\nu}(k_z', k_z, q, n) = \frac{2\pi}{\hbar}\left(N_q + \frac{1}{2} \pm \frac{1}{2}\right) \times E_a^2 \delta_{k_z', k_z \pm q} A_n^2 (q^2 + k_{l,n}^2)^2 |S_{\mu,\nu}(k_{l,n}, q_p)|^2 \times \delta[E_v(k_z') - E_\mu(k_z) \pm \hbar\omega_n(q)],$$

and

$$\delta[E_v(k_z') - E_\mu(k_z) \pm \hbar\omega_n(q)] = \sum_p \delta(q - q_p)/|\pm \partial[E_\nu(k_z \pm q_p) \pm \hbar\omega_n(q_p)]/\partial q|,$$

where $\text{JDOS}_\nu(q, k, q_p) = |\pm \partial[E_\nu(k_z \pm q_p) \pm \hbar\omega_n(q_p)]/\partial q|^{-1}$ is the charge-phonon joint density of states, n indicates a summation over phonon modes, p indicates summation over the roots of the equation $E_v(k_z') - E_\mu(k_z) \pm \hbar\omega_n(q) = 0$, which are represented by q_p above, and first $+/-$ in JDOS corresponds to forward/backward scattering and second $+/-$ corresponds to emission/absorption of a phonon. Given the nature of the confined dilatational acoustic phonons considered in our model, the above prescription for scattering through confined acoustic phonons is limited to intrasubband scattering.

For charge scattering through optical phonons, we have considered a bulk dispersionless optical phonon with $E_{op} = 63$ meV.[32] We have also utilized a scalar approximation for optical deformation potential, where the two transverse optical and the one longitudinal optical modes are taken into account. Although it has been mentioned that the scalar approximation is not accurate,[33] its utilization is however found to be widespread and to give results for mobility within 3% agreement with more detailed Monte Carlo simulations that take into account full symmetry of deformation potential.[34] The SiNW electron and hole momentum relaxation rates due to bulk optical phonons are given by

TABLE I. Equilibrium room temperature fractional hole occupancy ($\int_{1^{st}BZ} e^{-E_i(k_z)/k_B T} dk_z$) of the top four valence subbands for [110] SiNWs expressed in percent. N_i represents percentage occupancy in subband i.

Diameter (nm)	N_1	N_2	N_3	N_4
1.27	76.4	23.4	0.12	0.08
2.47	46.5	41.05	11.55	0.8
3.10	42.12	36.35	17.74	3.72

$$W_{\mu,\nu,\text{op}}(k_z) = \sum_{k_z',\tilde{\mathbf{q}}} W_{\mu,\nu,\text{op}}(k_z', k_z, \tilde{\mathbf{q}})\left(1 - \frac{k_z'}{k_z}\right) = -\frac{|D_{\text{op}}|^2}{4\pi\rho\omega_0} \delta_{k_z', k_z \pm q} \sum_{j=a,\text{em}} \frac{q_p}{k_z}\left[N(\hbar\omega_0) + \frac{1}{2} \pm \frac{1}{2}\right] \text{DOS}_{\nu,p}(k \pm q_p) \Gamma_{\mu,\nu}(k \pm q_p), \quad (20)$$

with

$$\Gamma_{\mu,\nu}(k \pm q_p) = \int_0^{q_c} q_t S_{1,\mu,\nu}(q_t, k_z \pm q_p) dq_t, \quad (21)$$

and

$$\text{DOS}_{\nu,p}(k \pm q_p) = |\partial[E_\nu(k_z \pm q_p)]/\partial q|^{-1}, \quad (22)$$

where q_p is the solution of $E_\mu(k_z \pm q_p) - E_\nu(k_z) \pm \hbar\omega_0 = 0$, $j = a, \text{em}$ indicates summation over phonon absorption or emission where possible, which includes both forward and backward transitions, $\text{DOS}_{\nu,p}$ is the density of states in final subband ν with the transition q_p, and $q_c \approx (1.9\pi/a)$ is used as an effective cut-off radius to emulate the projection of the BZ of bulk Si onto the confinement plane, much like the Debye approximation for bulk acoustic phonon scattering used above.

In computing the momentum relaxation rates using equations mentioned in this section, the following are specifically discussed:

(a) Electron—confined phonon acoustic intrasubband momentum relaxation rates for FSBC and CSBC for [110] and [100] SiNWs,
(b) Electron—bulk acoustic phonon inter- and intrasubband momentum relaxation rates for [110] SiNWs, and
(c) Hole—bulk optical phonon inter- and intrasubband momentum relaxation rates for [110] SiNWs.

Confined dilatational acoustic phonon modes are not sufficient to describe intersubband scattering and therefore intersubband scattering due to confined acoustic phonons are not discussed. Similarly, while hole intrasubband scattering due to confined optical phonons has been discussed elsewhere,[20] our calculations here show that intersubband scattering is important in these dimensionally reduced structures. This is because the percentage of equilibrium hole occupancy is non-negligible in the second and third valence subbands for [110] SiNWs at 300K, as shown in Table I. Therefore, for a

Downloaded 16 Sep 2008 to 129.97.106.193. Redistribution subject to AIP license or copyright; see http://jap.aip.org/jap/copyright.jsp

TABLE II. Equilibrium room temperature fractional electron occupancy of the bottom three conduction subbands for [110] SiNWs expressed in percent.

Diameter (nm)	N_1	N_2	N_3
1.27	99.9999	3.77×10^{-6}	6.44×10^{-7}
2.47	90.6	9.38	0.02
3.10	64.3	35.6	0.08

justifiable comparative analysis with hole-bulk acoustic phonon scattering, we consider hole-bulk optical phonon scattering that includes intersubband scattering. It is also necessary to point out that we assume that optical phonons are not effective in causing scattering of electrons in the conduction subbands. The justification for this stems from the fact that the deformation potential for intravalley scattering in bulk silicon due to optical phonons is assumed to be zero[7] (this is strictly valid only for the zero order term as shown in Ref. 35). The deformation potential for optical phonon scattering between valleys is usually assumed to be nonzero in bulk Si.[7] However for the SiNW with a diameter of 2.47 nm, the electron occupancy in the second conduction subband is small, as can be seen in Table II, and electron scattering due to optical phonons may be neglected for this SiNW. For the largest diameter SiNW considered, the occupancy of the second subband is about 34%. While neglecting electron scattering due to optical phonons between subbands 1 and 2 is questionable for this SiNW, we admit the neglect of this process and point that the electron mobility at room temperature is slightly overestimated for the 3.1 nm diameter SiNW. For larger diameter SiNWs, optical phonon scattering between subbands should be more carefully considered in future. The main point is that in spite of the overestimation of the electron mobility for the 3.1 nm diameter SiNW, the hole mobility, which is more accurate, is large.

Figures 5(a) and 5(b) depict total electron—acoustic phonon momentum relaxation rates at 300K for the lowest conduction subband for [110] SiNWs with diameters 1.27 and 2.47 nm, respectively. Three cases are considered—phonons confined in a box with a radius similar to the SiNW, phonons confined in a large 32 nm box, and bulk phonons. In calculating the momentum relaxation rates in Fig. 5, a value of 9.5 eV is used for the deformation potential.[29] As mentioned above, while momentum relaxation rates in Fig. 5 due to confined phonons are restricted to intrasubband transitions, intersubband transitions are considered in scattering due to bulk phonons. As can be seen, the large phonon box results very closely to resemble bulk phonon results, and provide verification for our bulk phonon scattering calculations. Moreover, as the SiNW diameter increases, the momentum relaxation rates difference between the equivalent radius phonon box and bulk phonons decreases. Peaks in the momentum relaxation rates due to confined phonons correspond to an electron transition to near the bottom of the subband after phonon emission. In the case of a phonon box of equivalent radius, there are relatively smaller numbers of phonon modes, resulting in a limited number of momentum relaxation rates peaks. However for a 32 nm phonon box, the

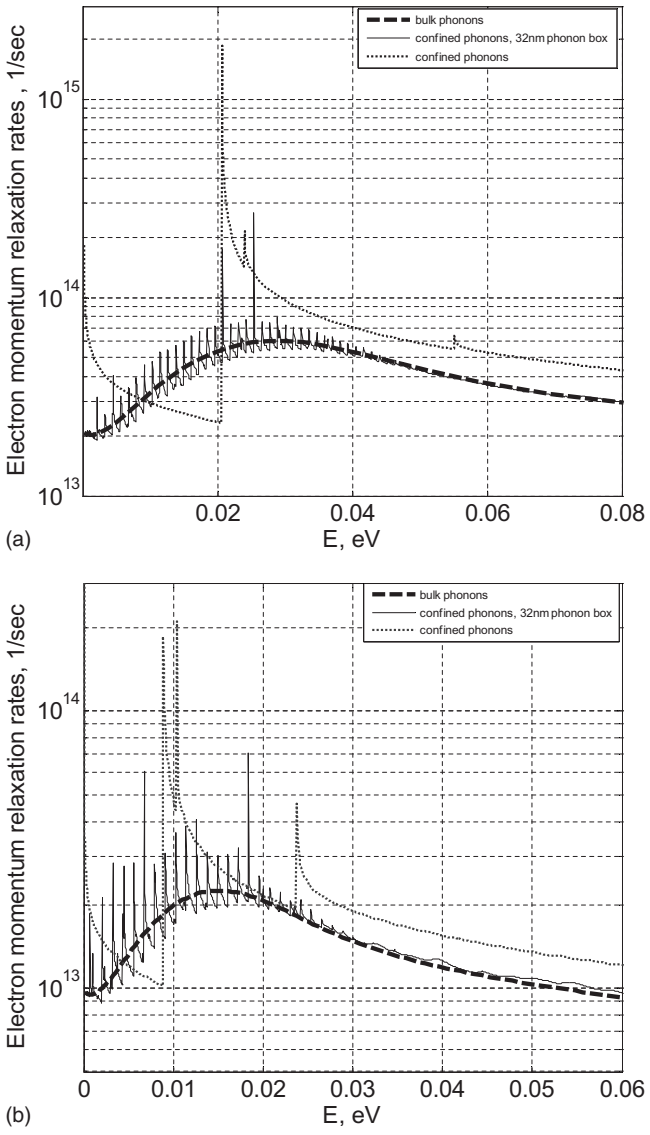
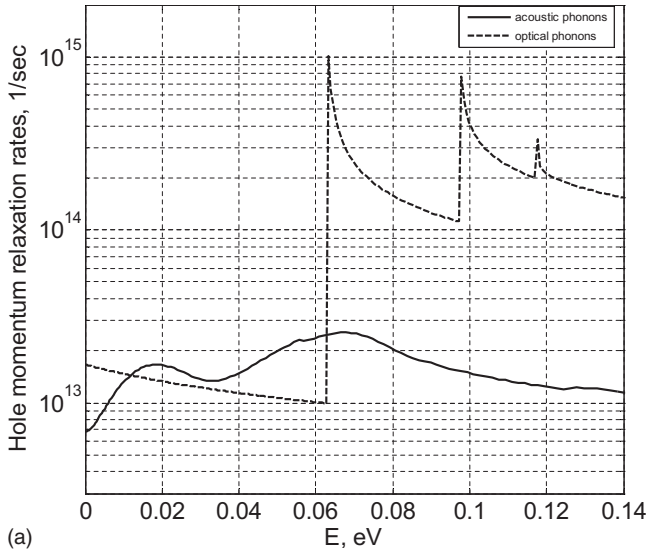


FIG. 5. (a) Lowest conduction subband electron-phonon momentum relaxation rates for a 1.27 nm diameter [110] SiNW. Intrasubband momentum relaxation rates from confined phonons are depicted, while intrasubband and intersubband rates from bulk phonons are depicted. (b) Lowest conduction subband electron-phonon momentum relaxation rates for a 2.47 nm diameter [110] SiNW. Intrasubband momentum relaxation rates from confined phonons are depicted, while intrasubband and intersubband rates from bulk phonons are depicted.

modes are significantly numerous, resulting in an equally larger number of momentum relaxation rate peaks closely spaced together. As one approaches the limit of a bulk phonon, this results in a quasicontinuum of peaks resulting in broad maxima.

Figures 6(a) and 6(b) depict hole-bulk acoustic and optical phonon momentum relaxation rates for [110] SiNWs with diameters 1.27 and 2.47 nm, respectively, for the highest valence subband. In computing the momentum relaxation rates for Fig. 6, an acoustic deformation potential value of 5 eV (Ref. 7) was used, and an optical deformation potential value of 13.24 eV/cm (Ref. 34) was used. As can be seen, hole-optical phonon scattering is significantly high at 300K, and strongly influences hole mobility. For the 1.27 nm SiNW, the first peak in the momentum relaxation rates due to

Downloaded 16 Sep 2008 to 129.97.106.193. Redistribution subject to AIP license or copyright; see http://jap.aip.org/jap/copyright.jsp



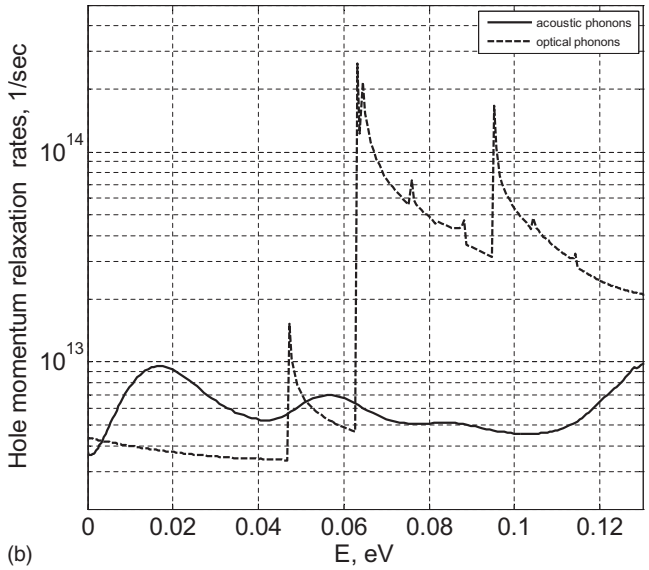


FIG. 6. (a) Highest valence subband hole-phonon momentum relaxation rates for a 1.27 nm diameter [110] SiNW. Intersubband scattering to top five valence subbands are considered. (b) Highest valence subband hole-phonon momentum relaxation rates for a 2.47 nm diameter [110] SiNW. Intersubband scattering to top five valence subbands are considered.

optical phonons corresponds to emission to the top of first valence band, while higher peaks correspond to absorption and emission to lower subbands. For the 2.47 nm SiNW, the situation is somewhat different, although broadly similar. The first peak corresponds to a hole transition to the third valence band by phonon absorption. The second peak is in effect two closely spaced peaks that correspond to hole transitions to the top of the first and second subbands. The two peaks are closely spaced because in this SiNW, the first and second valence subbands are nearly degenerate with a separation of approximately 1 meV at the $k_z=0$ point. Higher energy peaks correspond to absorption and emission into lower subbands.

Figure 7 shows electron momentum relaxation rates from acoustic phonons in case of CSBC for two different diameters of [110] SiNW. Just as in the FSBC, different peaks correspond to different phonon modes. One can also

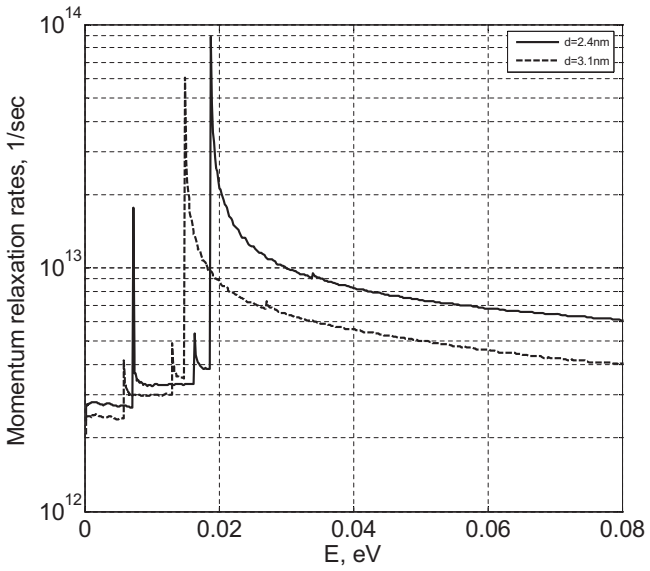


FIG. 7. Lowest subband electron momentum relaxation rates for clamped [110] SiNWs. Diameters are shown in the legend.

see from the figure that momentum relaxation rates are relatively strongly influenced by higher confined phonon $n=3$ mode. This is attributed to stronger interaction $\nabla\cdot\mathbf{u}$ [Eq. (18)], and is further illustrated in Fig. 8. Phonon modes greater than $n=3$ result in lower scattering, and play a smaller role in determining low-field mobility because of the high energy, and are therefore not depicted in Fig. 7.

III. MOBILITY

Electron and hole low-field mobility values are estimated based on momentum relaxation time approximation (MRTA) and given by

$$\mu = \frac{1}{\sum_i n_i} \sum_i \mu_i n_i, \tag{23}$$

where n_i is the charge carrier population in subband i, and

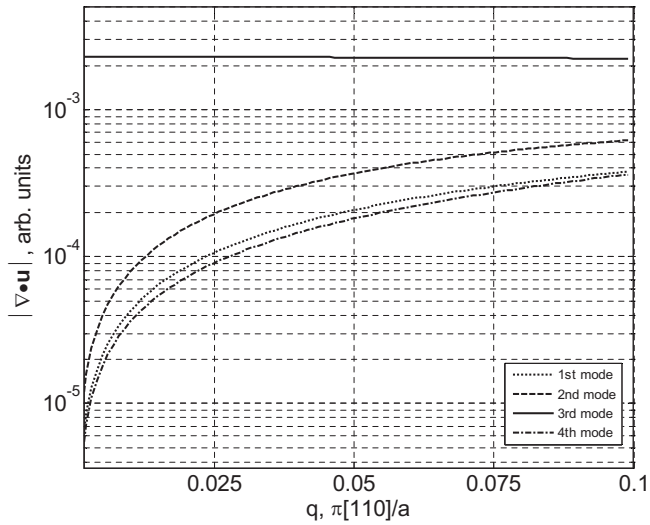


FIG. 8. Coupling strengths ($\nabla\cdot\mathbf{u}$) of first four phonon modes for a clamped 2.47 nm diameter [110] SiNW at $r=0$.

Downloaded 16 Sep 2008 to 129.97.106.193. Redistribution subject to AIP license or copyright; see http://jap.aip.org/jap/copyright.jsp

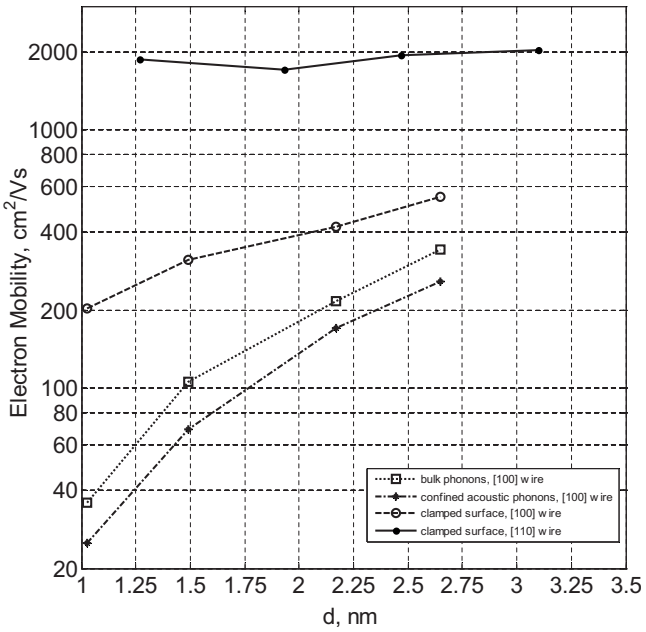


FIG. 9. Electron mobility for different SiNW boundary conditions, diameters, and axis.

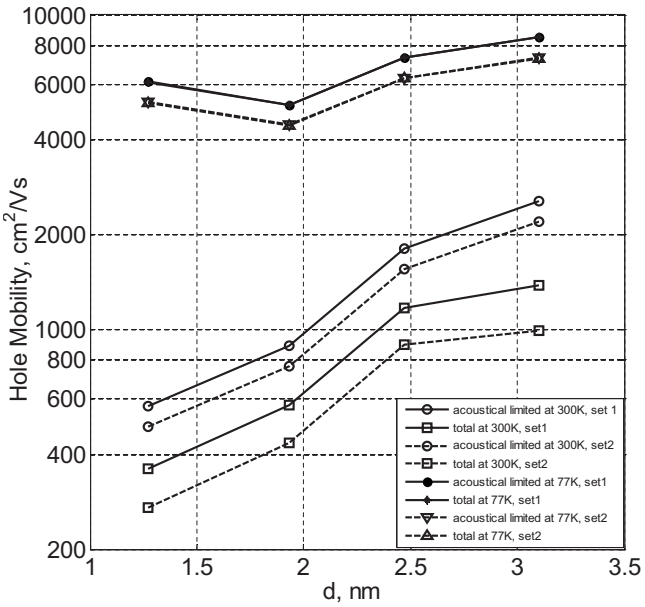


FIG. 10. Hole mobility for different [110] SiNWs with optical phonons and acoustical phonons at different temperatures. "Acoustic limited" mobilities are same as in Ref. 5.

$$\mu_i = \frac{2e}{k_B T m_{\text{eff}}} \frac{\int_{\text{first BZ}} E_i(k_z) W_i(k_z)^{-1} f_0(k_z) dk_z}{\int_{\text{first BZ}} f_0(k_z) dk_z}, \tag{24}$$

for each subband i, where $W_i(k_z) = \Sigma_\nu W_{i,\nu}(k_z)$ and $f_0(k_z) \approx e^{-(E_i/k_B T)}$. E_i is the electron/hole energy in subband i, measured with respect to the lowest/highest conduction/valence subband. An approximation in Eq. (24) is the use of effective mass of each subband at the band extrema. As a result, while the bandstructure is included in calculating scattering rates, it is not fully included in the calculation of the mobility. Future work will consider expressions for mobility which do not make this approximation.

Figure 9 depicts acoustic phonon limited electron low-field mobility versus diameter for [100] SiNWs at 300K for FSBC and CSBC as well as for bulk phonons, and low-field mobility in case of CSBC for [110] SiNWs. Comparing Fig. 9 with Ref. 5, one can clearly see that electron low-field mobility for [100] SiNWs is significantly lower than that of [110] SiNWs for all diameters considered. This is predominantly because of the relatively higher electron effective mass in [100] SiNWs compared to the [110] SiNWs. Also, one can see in Fig. 9 that in case of [110] SiNWs, CSBC results in almost no diameter dependence of electron low-field mobility. This may be understood in terms of the momentum relaxation rates depicted in Fig. 7, and discussed in Sec. II C. As can be seen, at low electron energies, which determine low-field mobility, there is a relatively smaller influence of the SiNW diameter on momentum relaxation rates compared to higher energies. However, for the [100] SiNWs, there is a comparatively greater diameter dependence of the low-field mobility for CSBC. This is attributed to a relatively large change in electron effective mass with respect to diameter for the [100] SiNWs compared to [110] SiNWs, as discussed in Sec. II A.

Figure 10 depicts hole low-field mobility versus [110] SiNW diameter for bulk acoustic phonons and total (acoustic+optical) phonons at 77 and 300K. The top three valence subbands are included in computing the hole mobility. Since deformation potential values vary somewhat in published literature, two different sets of deformation potential for hole acoustic and optical scattering are considered in Fig. 10. Set 1 from Ref. 34 has an acoustic deformation potential of 5.39 eV and an optical deformation potential of 13.24 eV/cm. Set 2 from Ref. 36 has an acoustic deformation potential of 5.0 eV and an optical deformation potential of 10.5 eV/cm. The difference in the hole mobility from the two sets is approximately 35% at 300K, and reduces to approximately 16% at 77K. This is primarily due to the negligible role of optical phonons in influencing low-field mobility at lower temperatures. At room temperature however, optical phonons reduce the mobility by as much as 50% in all the SiNWs considered for the two sets of deformation potential. As mentioned in Ref. 34 for bulk Si, the most accurate deformation potential values for these SiNWs may finally be obtained by comparing mobility with experimental data, which at this time are sparse. Irrespective of the deformation potential values set however, it can be seen in Fig. 10 that room temperature hole mobility is significantly higher than bulk silicon hole mobility of $\sim 450\ \text{cm}^2/\text{V s}$,[34] for the larger diameter SiNWs. At lower temperatures, however, this advantage in mobility over bulk silicon is lost.

For comparison purpose we have also evaluated electron and hole low-field mobility using relaxation time approximation (RTA). Table III provides a comparison between MRTA and RTA for the electron low-field mobility for confined and bulk acoustic phonons for freestanding [110] SiNWs. The degree of anisotropy in the electron scattering can be gauged

Downloaded 16 Sep 2008 to 129.97.106.193. Redistribution subject to AIP license or copyright; see http://jap.aip.org/jap/copyright.jsp

TABLE III. Calculated electron mobility for bulk and confined phonons at 300 K based on two approaches—RTA and MRTA.

Diameter (nm)	Confined, RTA ($cm^2/V\ s$)	Confined, MRTA ($cm^2/V\ s$)	Bulk, RTA ($cm^2/V\ s$)	Bulk, MRTA ($cm^2/V\ s$)
1.27	247	207	291	298
1.93	439	401	537	567
2.47	665	633	737	759
3.10	849	862	950	986

by comparing mobility based on the two approximations. If both mobility values are equal, this would suggest that we have an isotropic scattering. As can be seen in Table III, there is a small degree of anisotropy that is seen to decrease with diameter. With a further increase in diameter one may expect the scattering to become isotropic. As can also be seen from Table III as one takes larger diameter SiNWs, the difference between mobility due to confined and bulk acoustic phonons decreases. This is because of the reduced importance of phonon confinement at larger diameters, where higher confined phonon modes start to play a significant role as can be seen from the momentum relaxation rates in Fig. 5. While the first confined mode, which is linear, causes only backscattering (except at very low electron energies), higher modes result in both forward and backscattering as is in the case for bulk phonons. It may also be expected that the difference in mobility due to bulk and confined phonons may go down further with a further increase in diameter, and bulk phonons may be a relatively good approximation for some of the larger diameter freestanding SiNWs.

IV. SUMMARY

We have performed a comparative investigation of charge carrier-phonon interaction in [110] and [100] SiNWs ranging in diameter from 1 to 3 nm. The band structure has been obtained using a $sp^3d^5s^*$ TB scheme. Various phonons, bulk acoustic and optical, as well as confined acoustic phonons under FSBC and CSBC are considered. Momentum relaxation rates have been obtained using Fermi's golden rule and deformation potential approximation. In computing the momentum relaxation rates, TB electron and hole wave functions are utilized. Low-field mobility has also been computed using MRTA and RTA. [110] SiNWs are seen to have higher carrier mobility than [100] SiNWs because of the difference in effective mass. It is also found that while optical phonon scattering influences hole low-field mobility for the [110] SiNWs at room temperature, the total hole mobility is still higher than electron and bulk silicon hole mobility.

ACKNOWLEDGMENTS

We thank Professor David Janes (Purdue University) for suggesting the comparison of mobility results from different boundary conditions. We thank Md. Golam Rabbani for reading the manuscript and giving us useful feedback. We are grateful to the National Institute of Standards and Technology for supporting this work.

[1] X. Zhao, C. M. Wei, L. Yang, and M. Y. Chou, Phys. Rev. Lett. **92**, 236805 (2004).
[2] Y. Zhao and B. I. Yakobson, Phys. Rev. Lett. **91**, 035501 (2003).
[3] A. Svizhenko, P. W. Leu, and K. Cho, Phys. Rev. B **75**, 125417 (2007).
[4] Y. Wu, Y. Cui, L. Huynh, C. J. Barrelet, D. C. Bell, and C. M. Lieber, Nano Lett. **4**, 433 (2004).
[5] A. K. Buin, A. Verma, A. Svizhenko, and M. P. Anantram, Nano Lett. **8**, 760 (2008).
[6] D. Long, Phys. Rev. **120**, 2024 (1960).
[7] C. Jacoboni and L. Reggiani, Rev. Mod. Phys. **55**, 645 (1983).
[8] R. Mickevičius and V. Mitin, Phys. Rev. B **48**, 17194 (1993).
[9] B. K. Ridley, *Electrons and Phonons in Semiconductor Multilayers* (Cambridge University Press, Cambridge, England, 1997).
[10] N. Nishiguchi, Phys. Rev. B **54**, 1494 (1996).
[11] U. Bockelmann and G. Bastard, Phys. Rev. B **42**, 8947 (1990).
[12] S. Yu, K. W. Kim, M. A. Stroscio, G. J. Iafarte, and A. Ballato, Phys. Rev. B **50**, 1733 (1994).
[13] M. A. Stroscio and M. Dutta, *Phonons in Nanostructures* (Cambridge University Press, Cambridge, England, 2005).
[14] R. Kotlyar, B. Obradovic, P. Matagne, M. Stettler, and M. D. Giles, Appl. Phys. Lett. **84**, 5270 (2004).
[15] A. Svizhenko, S. Bandyopadhyay, and M. A. Stroscio, J. Phys.: Condens. Matter **10**, 6091 (1998).
[16] M. A. Stroscio and K. W. Kim, Phys. Rev. B **48**, 1936 (1993).
[17] S. Jin, M. V. Fischetti, and T. Tang, J. Appl. Phys. **102**, 083715 (2007).
[18] F. Comas, A. Cantarero, C. Trallero-Giner, and M. Moshinsky, J. Phys.: Condens. Matter **7**, 1789 (1995).
[19] N. C. Constantinou and B. K. Ridley, J. Phys.: Condens. Matter **1**, 2283 (1989).
[20] M. Nawaz, J. P. Leburton, and J. Jin, Appl. Phys. Lett. **90**, 183505 (2007).
[21] G. D. Sanders, C. J. Stanton, and Y. C. Chang, Phys. Rev. B **48**, 11067 (1993).
[22] Y. Cui, Z. Zhong, D. Wang, W. U. Wang, and C. M. Lieber, Nano Lett. **3**, 149 (2003).
[23] J. M. Jancu, R. Scholz, F. Beltram, and F. Bassani, Phys. Rev. B **57**, 6493 (1998).
[24] Y. Zheng, C. Rivas, R. Lake, K. Alam, T. B. Boykin, and G. Klimeck, IEEE Trans. Electron Devices **52**, 1097 (2005).
[25] R. M. Martin, *Electronic Structure, Basic Theory and Practical Methods* (Cambridge University Press, Cambridge, England, 2004).
[26] D. Royer and E. Dieulesaint, *Elastic Waves in Solids I* (Springer, New York, 2000).
[27] V. A. Fonoberov and A. A. Balandin, Nano Lett. **6**, 2442 (2006).
[28] M. A. Stroscio, K. W. Kim, S. Yu, and A. Ballato, J. Appl. Phys. **76**, 4670 (1994).
[29] M. Lundstrom, *Fundamentals of Carrier Transport*, 2nd ed. (Cambridge University Press, Cambridge, England, 2000).
[30] U. Rössler, *Solid State Theory* (Springer, New York, 2004).
[31] S. Yu, K. W. Kim, M. A. Stroscio, G. J. Iafrate, and A. Ballato, J. Appl. Phys. **80**, 2815 (1996).
[32] J. M. Hinckley and J. Singh, J. Appl. Phys. **76**, 4192 (1994).
[33] K. Reimann, R. A. Kaindl, and M. Woerner, Phys. Rev. B **65**, 045302 (2001).
[34] M. V. Fischetti and S. E. Laux, J. Appl. Phys. **80**, 2234 (1996).
[35] W. A. Harrison, Phys. Rev. **104**, 1281 (1956).
[36] T. Yamada and D. K. Ferry, Solid-State Electron. **38**, 881 (1995).

Downloaded 16 Sep 2008 to 129.97.106.193. Redistribution subject to AIP license or copyright; see http://jap.aip.org/jap/copyright.jsp